

# A compact microscope setup for multimodal nonlinear imaging in clinics and its application to disease diagnosticst

Cite this: *Analyst*, 2013, **138**, 4048

Tobias Meyer,<sup>a</sup> Martin Baumgartl,<sup>b</sup> Thomas Gottschall,<sup>b</sup> Torbjörn Pascher,<sup>cd</sup> Andreas Wuttig,<sup>a</sup> Christian Matthäus,<sup>a</sup> Bernd F. M. Romeike,<sup>e</sup> Bernhard R. Brehm,<sup>f</sup> Jens Limpert,<sup>b</sup> Andreas Tünnermann,<sup>bg</sup> Orlando Guntinas-Lichius,<sup>h</sup> Benjamin Dietzek,<sup>ai</sup> Michael Schmitt<sup>i</sup> and Jürgen Popp<sup>\*ai</sup>

The past years have seen increasing interest in nonlinear optical microscopic imaging approaches for the investigation of diseases due to the method's unique capabilities of deep tissue penetration, 3D sectioning and molecular contrast. Its application in clinical routine diagnostics, however, is hampered by large and costly equipment requiring trained staff and regular maintenance, hence it has not yet matured to a reliable tool for application in clinics. In this contribution implementing a novel compact fiber laser system into a tailored designed laser scanning microscope results in a small footprint easy to use multimodal imaging platform enabling simultaneously highly efficient generation and acquisition of second harmonic generation (SHG), two-photon excited fluorescence (TPEF) as well as coherent anti-Stokes Raman scattering (CARS) signals with optimized CARS contrast for lipid imaging for label-free investigation of tissue samples. The instrument combining a laser source and a microscope features a unique combination of the highest NIR transmission and a fourfold enlarged field of view suited for investigating large tissue specimens. Despite its small size and turnkey operation rendering daily alignment dispensable the system provides the highest flexibility, an imaging speed of 1 megapixel per second and diffraction limited spatial resolution. This is illustrated by imaging samples of squamous cell carcinoma of the head and neck (HNSCC) and an animal model of atherosclerosis allowing for a complete characterization of the tissue composition and morphology, *i.e.* the tissue's morphochemistry. Highly valuable information for clinical diagnostics, *e.g.* monitoring the disease progression at the cellular level with molecular specificity, can be retrieved. Future combination with microscopic probes for *in vivo* imaging or even implementation in endoscopes will allow for *in vivo* grading of HNSCC and characterization of plaque deposits towards the detection of high risk plaques.

Received 19th February 2013

Accepted 2nd April 2013

DOI: 10.1039/c3an00354j

[www.rsc.org/analyst](http://www.rsc.org/analyst)

## Introduction

Multimodal nonlinear microscopy combining the effects of second harmonic generation (SHG), two-photon excited

fluorescence (TPEF) and coherent anti-Stokes Raman scattering (CARS) for label-free imaging of native tissues has gained much interest during the past years as a versatile imaging tool in fundamental research on diseases.<sup>1–4</sup> This is due to the unique

<sup>a</sup>Institute of Photonic Technology Jena IPHT, Albert-Einstein-Strasse 9, 07745 Jena, Germany. E-mail: [juergen.popp@iphj-jena.de](mailto:juergen.popp@iphj-jena.de); Fax: +49 3641206399; Tel: +49 3641206300

<sup>b</sup>Institute of Applied Physics and Abbe Center of Photonics, Friedrich-Schiller-University Jena, Albert-Einstein-Str. 15, 07745 Jena, Germany. E-mail: [jens.limpert@uni-jena.de](mailto:jens.limpert@uni-jena.de); Fax: +49 3641947802; Tel: +49 3641947811

<sup>c</sup>Pascher Instruments AB, Stora Rabybyväg 24, 22478 Lund, Sweden

<sup>d</sup>Department of Chemical Physics Lund University, Kemiceriet, Gatingevägen 60, 22241 Lund, Sweden. E-mail: [Torbjorn.Pascher@chemphys.lu.se](mailto:Torbjorn.Pascher@chemphys.lu.se); Fax: +46 46134155; Tel: +46 46134155

<sup>e</sup>Institute of Pathology, Department of Neuropathology, Jena University Hospital – Friedrich-Schiller-University, Erlanger Allee 101, 07740 Jena, Germany. E-mail: [Bernd.Romeike@med.uni-jena.de](mailto:Bernd.Romeike@med.uni-jena.de); Fax: +49 36419324752; Tel: +49 36419324755

<sup>f</sup>Catholic Clinic – Koblenz, Internal Medicine & Cardiology, Rudolf Virchow Str. 9, 56073 Koblenz, Germany

<sup>g</sup>Fraunhofer Institute for Applied Optics and Precision Engineering, Albert-Einstein-Str. 7, 07745 Jena, Germany. E-mail: [andreas.tuennermann@iof.fraunhofer.de](mailto:andreas.tuennermann@iof.fraunhofer.de); Fax: +49 3641807600; Tel: +49 3641807201

<sup>h</sup>Department of Otorhinolaryngology, University Hospital, Lessingstr. 2, 07743 Jena, Germany. E-mail: [orlando.guntinas@med.uni-jena.de](mailto:orlando.guntinas@med.uni-jena.de); Fax: +49 3641935129; Tel: +49 3641935127

<sup>i</sup>Institute of Physical Chemistry and Abbe Center of Photonics, Friedrich-Schiller-University Jena, Helmholtzweg 4, 07743 Jena, Germany. E-mail: [juergen.popp@uni-jena.de](mailto:juergen.popp@uni-jena.de); Fax: +49 3641948302; Tel: +49 3641948320

† Electronic supplementary information (ESI) available: S1 and S2 contain detailed information on the optical layout of the instrument as well as the design of the hardware electronics and software. See DOI: 10.1039/c3an00354j

set of properties in comparison to the established biomedical visualization methods like *e.g.* MRI, ultrasound and X-ray tomography, which render multimodal nonlinear imaging particularly powerful for disease diagnostics. Nonlinear microscopy utilizing near infrared (NIR) laser wavelengths provides label-free molecule specific image contrast combined with diffraction limited spatial, *i.e.* lateral and axial, resolution for accessing depths of up to 1 mm in scattering tissues<sup>5,6</sup> with video rate image acquisition.<sup>7</sup> It has been demonstrated for a wide range of clinical patterns that similar information about the tissue morphology and composition is accessible by SHG/TPEF/CARS multimodal imaging as compared to the golden standard of *ex vivo* histopathology using multiple staining agents and immunohistochemical markers, *e.g.* for brain tumors,<sup>8–10</sup> colon<sup>11</sup> and skin cancer.<sup>12</sup> CARS microscopy is particularly useful for investigating diseases associated with lipid metabolism.<sup>13</sup> The most prominent diseases related to lipid biology are cardiovascular diseases (CVDs). CVDs account for more than 40% of deaths in Germany,<sup>14</sup> constituting the leading cause of death worldwide. Atherosclerosis is the most prevalent among the manifold manifestations of cardiovascular diseases. Though disease progression is influenced by many risk factors and its abundance increases with age, in particular in the case of atherosclerosis the disease development is initiated as early as in the second or third decade of life<sup>15</sup> and therefore there is sufficient time for treatment to mitigate the etiopathology. However, to do so early recognition in the absence of unambiguous symptoms is required. Atherosclerosis is a chronic disease of the arteries resulting in deposition of lipid plaques at the vessel wall. Therefore early diagnosis when the plaque burden is still low is very important to abort the disease. But the visualization of lipid deposits within arteries alone is insufficient, since the pathological behaviour of a plaque is not only dependent on its size but more importantly on its molecular composition.<sup>16</sup> Hence, imaging tools providing insight into the plaque's morphology and its chemical composition are required, ideally allowing for a non-invasive or minimally invasive routine screening of patients. Vulnerable plaques, *i.e.* plaques of high risk to rupture, are characterized by large lipid cores, thin fibrous caps and surrounding inflammatory cell infiltrates.<sup>15,16</sup> These structures serving as disease markers can be visualized by nonlinear imaging combining SHG, TPEF and CARS. SHG is particularly sensitive to collagen fibers and cholesterol,<sup>17–19</sup> whereas TPEF visualizes the distribution of autofluorescent protein fibers, *e.g.* collagen and elastin, in the vessel wall<sup>20,21</sup> and oxidized fatty acids within the plaques.<sup>22</sup> CARS is capable of determining the spatial distribution of in principle any Raman active molecule by exciting characteristic vibrational resonances. However, CARS is mostly used to visualize the lipid distribution at  $2850\text{ cm}^{-1}$  corresponding to the symmetric C–H-stretching vibration of methylene groups,<sup>23</sup> which is not a unique structural characteristic of lipids, but in contrast to other major biomolecules highly abundant in lipids. Though the prospects of multimodal nonlinear imaging as a clinical imaging tool are recognized for investigating multiple disease patterns, *e.g.* cancer<sup>3,8–12</sup> and lipid metabolism related diseases<sup>13</sup> such as atherosclerosis,<sup>24–28</sup> its

widespread application is limited to fundamental research and has not yet spread to clinical routine diagnostics due to instrumental complexity of the apparatus. The state of the art multimodal imaging platform<sup>20,29,30</sup> is based on a commercial laser scanning microscope utilizing a two colour tunable ultrafast laser, typically consisting of an 80 MHz repetition rate laser combined with an optical parametric oscillator (OPO): the OPO generates by frequency conversion the second tuneable laser wavelength required for CARS imaging. Hence, multimodal imaging platforms require large laser systems and sophisticated microscopes controlled by complex data acquisition hard- and software. Therefore, apart from high costs, instrument handling is difficult and requires trained staff for maintenance. In addition subtle changes in the environment, *e.g.* temperature or humidity, may require realignment of the setup. Thus the currently available equipment is not compatible with routine application in clinics, *e.g.* at the patient's bedside or in an operation theatre. Furthermore for 80 MHz laser systems there is a clear discrepancy between high spectral resolution requiring ps-lasers in the case of CARS and high peak power optimal for SHG and TPEF imaging requiring fs-lasers.<sup>24,30</sup> Hence either SHG and TPEF excitation efficiency is sacrificed by using ps-lasers,<sup>25</sup> or the spectral resolution of CARS is reduced by using fs lasers<sup>30</sup> or the instrument complexity and image acquisition time are significantly increased by subsequently using fs and ps lasers for efficiently exciting TPEF, SHG and CARS signals.<sup>24</sup>

Fiber laser based approaches for generating multicolour laser beams appear to be most promising in order to reduce instrument size and alignment requirements. Here several concepts for in-fiber frequency conversion have been introduced: supercontinuum generation,<sup>26,31</sup> soliton self-frequency shift<sup>32,33</sup> and four-wave mixing (FWM).<sup>34</sup> However, supercontinuum generation results in spectrally broadband emission but low spectral power density requiring additional filtering for single band CARS. Soliton self-frequency shift on the other hand generates red shifted radiation but requires short pulses. Only the four-wave mixing process is compatible with high spectral resolution and long pulse duration, which simplifies the alignment of the temporal pulse overlap. FWM furthermore allows for wavelength tuning by either tuning the pump wavelength or by seeding the FWM process which in addition increases the spectral resolution.<sup>34,35</sup> Just recently novel all-fiber laser sources have been developed and successfully applied to multimodal nonlinear microscopy<sup>36–38</sup> generating synchronized laser radiation in a photonic crystal fiber by four-wave mixing (FWM), however only proof of principle of operation has been so far demonstrated.

In this contribution a novel compact setup for multimodal nonlinear imaging suited for clinical diagnostics is presented. The system features a fourfold enlarged field of view along with the highest NIR transmission of 60% from the laser onto the specimen, which enables using alignment-free ultracompact low power multi-colour fiber lasers. Despite the reduced size, the instrument's performance in terms of imaging speed, image contrast and spatial resolution is comparable to commercially available laser scanning microscopes in combination with

solid-state lasers. This system is suited to investigate a variety of disease patterns, in particular the most prevalent ones such as cardiovascular diseases and cancer. In order to demonstrate the instrument's capabilities for biomedical imaging *ex vivo* samples of an animal model for atherosclerosis, human perivascular tissue as well as a specimen of a carcinoma of the oropharynx have been investigated and the results are presented in the following. Due to the instruments compactness, simplicity and high image quality the microscopic platform represents a significant step towards establishing multimodal nonlinear imaging in clinical settings, hence application of this device to routine clinical imaging as a diagnostic tool is anticipated in the near future while further technological research will focus on multimodal endoscopy.

## Materials and methods

A schematic sketch of the compact microscope setup for multimodal nonlinear imaging is displayed in Fig. 1 panel A, while photographs of the setup shown in panels B through E provide a realistic impression of the system's size.

### 1 NIR fiber laser

A key element for constructing a small size and portable nonlinear microscope is the application of an ultracompact and portable laser light source. The multicolour fiber laser used is a customized design for CARS, TPEF and SHG microscopy based on an amplified ytterbium fiber laser of 1.9 MHz repetition rate and 51 ps pulse duration<sup>37</sup> spliced to a photonic crystal fiber PCF similar to the designs previously reported.<sup>36,38</sup> Such a fiber

laser is shown in panel E of Fig. 1 (Active Fiber Systems, Germany). The PCF has been chosen such that the frequency difference between the FWM signal wavelength and the fundamental pump wavelength corresponds to the vibrational frequency of the symmetric C–H-stretching vibration of methylene groups, *i.e.*  $2850\text{ cm}^{-1}$ . For CARS both the FWM signal and ytterbium fundamental pulses have been used for imaging, while for SHG and TPEF excitation the ytterbium fundamental wavelength of 1032 nm has been used. The signal pulse train used as the CARS pump is centred at 797 nm. The pulse duration is 19 ps providing a spectral width of  $40\text{ cm}^{-1}$  full width at half maximum (FWHM) and a power of 25 mW. The ytterbium pump laser used as the Stokes beam in the CARS process is spectrally located at 1032 nm, providing more than 100 mW power and a spectral width of  $6\text{ cm}^{-1}$  FWHM, which is attenuated to 20 mW for imaging. The wavelength set of this laser is furthermore within the optimal window for tissue imaging, minimizing losses due to scattering and absorption, *i.e.* between the lowest electronic absorption of haemoglobin and the highest vibrational absorption bands of water. This wavelength region spans the range from 750 nm to 1500 nm. For imaging at maximum 30 mW of pump and Stokes power were focused onto the sample using a  $20\times$  NA 0.4 objective.

### 2 Compact nonlinear laser scanning microscope

The microscope design has been optimized to realize high optical throughput, hence the number of optical elements is minimized without affecting the optical performance, *i.e.* diffraction limited spatial resolution. In comparison to commercial laser scanning microscopes used in alternative multimodal microscopes,<sup>8,9</sup> the optical layout of the microscope as displayed in Fig. 2 panel A provides a fourfold increased field of view for SHG/TPEF/CARS microscopy of large tissue samples by designing a short focal distance scan lens of only 70 mm featuring achromatic correction from 750 to 1100 nm and minimized reflection up to 1550 nm. A NIR transmission of the illumination beam path of 60% from the laser onto the specimen is realized, which is larger than the NIR transmission of

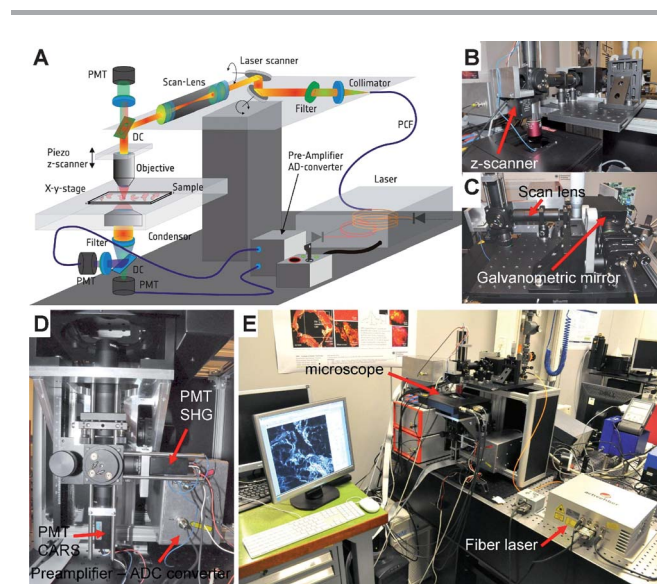


**Fig. 1** Schematic sketch of the complete nonlinear microscope (panel A) and photographs of the experimental setup (panels B–E). The footprint of the microscope is  $60\text{ cm} \times 45\text{ cm}$  enabling assembly also in areas with limited space. The illumination part of the microscope and the epidetection path are imaged in panels B and C. In panel D the optics and PMT detectors in the forward direction are displayed. The box on the right contains the preamplifier and analogue-to-digital converter for processing the signals from the PMT detectors. The overview image in panel E shows the computer for system control, the laser and the microscope.

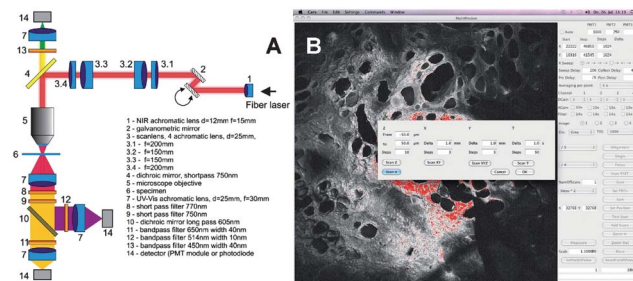


**Fig. 2** Panel A: scheme of the optical layout of the multimodal nonlinear microscope for simultaneous detection of SHG, TPEF and CARS signals. Manufacturers of the optical components: 1, 3, 4 – Edmund optics, USA; 7, 11, 12, 13 – Thorlabs, USA; 8, 9 – Semrock, USA. Panel B: screen shot of the graphical user interface for controlling the nonlinear microscope. All elements for system control are displayed. When performing a multiple image scan, the menu in the center allows choosing one of the 4 options for scanning multiple images, *i.e.* time series, *z*-, *xy*- and *xyz*-scans.

alternative CARS imaging platforms providing NIR transmission ranging from 10% (ref. 39) to 40%.<sup>40</sup> This configuration enables using relatively low power but ultra-compact, robust and maintenance free fiber lasers described in the preceding section. Since nonlinear imaging methods provide 3D sectioning, no confocal microscope design is required. The instrument is described in detail in the ESI.† For the separation of the nonlinear signals from residual laser light in the forward direction two short pass filters are used (SP770 and SP750, Semrock, USA). The forward emitted SHG and CARS signals are split by a longpass dichroic mirror (LP605, 24 mm × 36 mm, Thorlabs, USA), filtered by appropriate bandpass filters (CARS: bandpass 650/40 Thorlabs, SHG: bandpass 400/40 or 514/10, Thorlabs, USA) before being detected by PMT modules (Hamamatsu, Japan). TPEF or alternatively backward scattered CARS/SHG signals are detected in epi-direction. In order to optimize the detection efficiency of the low intensity signals, the distance between the sample and detectors is minimized in order to improve the collection of multiply scattered photons. The whole system is schematically depicted in Fig. 1 panel A, while panels B–E show photographs of parts of the system. The arrangement of the optical elements is illustrated in Fig. 2 panel A.

### 3 Data acquisition hardware and graphical user interface

The data acquisition soft- and hardware has been designed for controlling the galvanometric mirrors, the motorized *xy* microscope translation stage and the piezo *z*-focussing stage in addition to synchronized data acquisition of up to four channels simultaneously. The data acquisition system consists of two parts: the first part is a small desktop computer for running the graphical user interface for complete instrument control *via* USB and storage of the image data and the second device is the data acquisition hardware unit controlling the instrument, designed by T. P., Pascher Instruments AB, Sweden. The menus of the graphical user interface are clearly arranged in order to provide intuitive but complete control of the hardware. A screenshot of the software is displayed in Fig. 2 panel B.

As indicated in the screenshot shown in Fig. 2, four options are available: a time series scan for investigating dynamic processes, *z*-scan for depth resolved imaging of thick samples, *xy*-scan using the motorized stage for analysing sample areas exceeding the field of view of the scanner and *xyz*-scans for investigating extended thick specimens.

The key aspect for adaptation of the electronics' hardware of the instrument to nonlinear imaging is to optimize the detection system towards highly efficient and low noise acquisition of low intensity signals. This has been realized by using 16 bit data depth, which allows using the full dynamic range of a PMT module of 3 orders of magnitude in intensity to detect simultaneously weak and bright structures, thus enabling analysis of small intensity fluctuations and avoiding loss of information due to analogue-to-digital conversion. In addition a large set of averaging options, *e.g.* pixel dwell times of up to 256  $\mu$ s and averaging of a specific number of frames as well as additional electronic low pass filtering and pre-amplification preceding analogue-to-digital conversion have been implemented. The

**Table 1** Summary of specifications of the multimodal nonlinear microscope

Parameter	Custom built LSM
Field of view 20×	1.2 × 1.2 mm <sup>2</sup>
Scanning speed @ 1024 <sup>2</sup>	2 s
NIR T[%] 800/1000 nm	>60%
Image size, pixels	128 × 128 to 4096 × 4096
Pixel dwell time	1 $\mu$ s to 256 $\mu$ s
Data depth	16 bit

in-depth description of the data acquisition hardware design can be found in the ESI section.† The most important parameters of the hardware control unit are summarized in Table S2.†

In summary key imaging specifications of the instrument are collected in Table 1.

### 4 Investigated tissue samples

Adult male New Zealand white rabbits (Harlan, Borchon, Germany) were fed with a 0.5% cholesterol diet to initiate atherosclerotic plaque deposition. The rabbits were sacrificed by an overdose of an anaesthetic solution of ketamine and xylazine. The aortic artery was excised and preserved in 5% formalin solution (Oscar Fischer GmbH, Saarbrücken, Germany), either for *in vitro* non-linear imaging or preparation of 5  $\mu$ m cross-sections using a microtome. For preparing thin dried tissue sections no standard embedding medium has been used to avoid signal contributions from the embedding matrix. The cross-sections were placed on CaF<sub>2</sub> slides. For *in vitro* multimodal imaging of plaque deposits at the inner arterial wall the blood vessel was cut open, immersed in physiological buffer and sandwiched between two microscope coverslips, thus avoiding denaturation and shrinkage during the measurement.

For determining contrast and as a control tissue human tissue was investigated. The specimen was obtained from routine biopsy at the University hospital, Jena, Germany.

The section of a head and neck squamous cell carcinoma (HNSCC) sample was obtained from a biopsy of the left tonsil of a patient with pT3N2bM0 carcinoma. The biopsy specimen was taken from the primary tumor site and its environment. A cryosection of 20  $\mu$ m thickness was investigated without further tissue processing. Usage of material from routine biopsies was approved by the ethics committee for human research at the Medical Faculty, Friedrich-Schiller-University Jena, Germany.

### 5 Image analysis

For image analysis ImageJ<sup>41</sup> has been used.

## Results and discussion

In comparison to multimodal imaging platforms based on highly integrated commercial laser scanning microscopes in combination with solid-state ultrafast lasers,<sup>9,18,26,30</sup> the presented homebuilt microscopic setup can be quickly moved and reinstalled, provides the highest NIR transmission of 60%, a

high flexibility by direct access to all optical and mechanical elements and an enlarged field of view (FOV). Due to the custom optical layout of the scan lens the FOV of the homebuilt instrument is four times larger enabling faster investigation of extended tissue specimens as illustrated in Fig. 3 panel A. Here a CARS image at  $2850\text{ cm}^{-1}$  of an aorta cross-section of an animal model for atherosclerosis is displayed. The large white box marks the FOV of this microscope in combination with a  $20\times$  objective, while the small dashed square corresponds to the FOV of a standard commercial laser scanning microscope used in previous multimodal nonlinear imaging investigations.<sup>9</sup>

The small footprint allows installation in areas with space constraints. While most laser scanning systems are installed at a fixed position on laser tables due to the large ultrafast lasers, the setup here can be disassembled and reconstructed within a few hours. Most commercial laser scanning systems used for nonlinear microscopy are based on confocal instruments initially designed for fluorescence microscopy using visible

lasers. This results in limited NIR transmission<sup>39</sup> in comparison to 60% as reported herein and unnecessary complexity of the instrument, *e.g.* integrated internal descanned confocal detectors. A confocal detection design limits the system to the detection of ballistic signal photons only, which is, with tissue depth, an exponentially decreasing fraction of all generated signal photons. The instrument described herein has no confocal design thus reducing the instruments complexity and improving the overall transmission. The lateral and axial resolution is not reduced, since nonlinear microscopy provides intrinsically 3D sectioning with *xyz*-resolution comparable to confocal microscopy.<sup>5,42</sup>

Another major benefit of the instrument is related to the novel turn-key and small footprint fiber laser light source characterized by low repetition rate and long, *i.e.* tens of ps, pulse duration. As can be seen in Fig. 1 panel E, the size of the laser is significantly smaller than a conventional laser source for CARS microscopy. The simultaneous emission of the long duration, *i.e.* tens of ps temporal pulse width, ytterbium fundamental and the FWM signal and idler wavelengths from the same small core fiber end results in perfect spatial and temporal overlap of pump and Stokes wavelengths rendering daily alignment dispensable and is a unique feature of only this laser concept. In contrast to alternatively used ultrafast solid-state laser systems applied to multimodal nonlinear imaging, *e.g.* either two synchronized oscillators,<sup>24,25</sup> a single oscillator in combination with an optical parametric oscillator (OPO),<sup>30,43</sup> or single broadband laser sources incorporating free space optics and pulse shapers,<sup>44</sup> which require regular adjustment, this laser is designed for maintenance free operation. Also alternative compact fiber laser concepts based on soliton self-frequency shift,<sup>32,33</sup> supercontinuum generation,<sup>26,31</sup> four-wave mixing,<sup>34–38</sup> a fiber optic parametric oscillator<sup>45</sup> or two synchronized ps fiber lasers<sup>40</sup> still rely on mechanical delay lines and dichroic mirrors to overlap pump and Stokes pulses temporally and spatially, which results in higher sensitivity to environmental changes and regular adjustment in contrast to the fully fiber integrated approach presented here. In particular except for the concept of two synchronized ps fiber lasers,<sup>40</sup> all other laser sources are based on much shorter pulses, hence pulse dispersion in the microscope optics results in a significant temporal walk off of the pulses, which needs to be corrected for by the mechanical delay and adjusted, when changing the objective. Due to the longer pulse duration of several tens of ps of the laser presented herein,<sup>37</sup> the velocity difference between pump and Stokes pulses in the microscope optics results only in a negligible temporal walk off of a small fraction of the pulse length and therefore the temporal pulse overlap is always preserved. This laser characteristic enables to greatly simplify the microscope optics, in particular the number of optical elements can be reduced, and thus is the key to improve the overall NIR transmission as described in the preceding section.

Furthermore, commercial CARS lasers of 80 MHz repetition rate and ps pulse duration excite SHG and TPEF signals less effectively.<sup>24,46</sup> On the other hand, fs lasers of 80 MHz repetition rate provide efficient SHG and TPEF excitation but come at the cost of a poor spectral resolution of only  $100\text{ cm}^{-1}$  for CARS

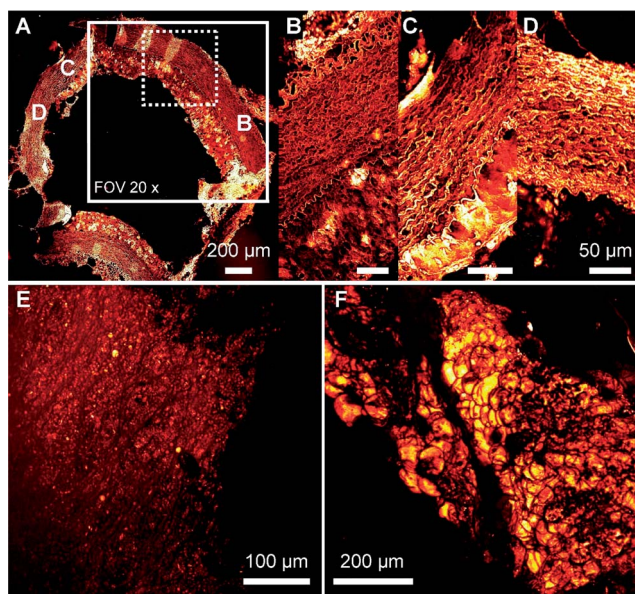


**Fig. 3** CARS imaging of tissue samples from an animal model for atherosclerosis, *i.e.* a rabbit fed with a high cholesterol diet for several weeks. Imaging was performed at the symmetric aliphatic C–H-stretching vibration of methylene groups,  $2850\text{ cm}^{-1}$ . In panel A the large field of view (FOV) of the customized microscope is indicated as a white square, while the small dashed square corresponds to the FOV of a commercial standard laser scanning microscope. Especially for medical use orientation on large specimens is improved due to a larger FOV. For investigating areas of several mm extension, multiple images obtained by *xy* translation of the sample are fused as in the case of the whole artery cross-section, panel A. In panels B, C and D areas of different plaque deposition are displayed as indicated in panel A. The curly elastic protein fiber strands of the arterial wall are clearly visualized, as well as the lipid deposits and their structure at the inner vessel wall. Different brightness indicates that the plaque composition varies, since the concentration of methylene groups is visualized. In panels E and F the microscopes *z*-scanning option and deep tissue penetration of the NIR laser are demonstrated by imaging of plaque deposits from the lumen of the artery in buffer solution and detecting the CARS signal through  $500\text{ }\mu\text{m}$  of tissue in the forward direction. In panel E an area of low plaque deposition is shown, the depth of this *z*-projection corresponds to  $40\text{ }\mu\text{m}$ . In panel F a lipid deposit of  $100\text{ }\mu\text{m}$  thickness is displayed.

imaging.<sup>30</sup> Additionally due to the much shorter pulse duration temporal walk off of the fs-pulses as well as group velocity dispersion significantly complicate the alignment. The peak power of the laser used in this work<sup>37</sup> is the same as for a 500 fs laser system of 80 MHz repetition rate but provides a spectral resolution better than  $40\text{ cm}^{-1}$  for the pump and below  $6\text{ cm}^{-1}$  for the Stokes wavelength. As previously reported, the spectral resolution can be further increased to  $1\text{ cm}^{-1}$ , when the FWM process is seeded<sup>35</sup> using a continuous wave (cw) laser. Here spectral tuning in the range from  $1200$  to  $3800\text{ cm}^{-1}$  with a small gap around  $2000\text{ cm}^{-1}$  has been realized, which compares well with alternative tunable fiber lasers.<sup>32,34,40</sup> However, in order to minimize the system's complexity, we operate the fiber laser at a fixed spectral position tuned to be in resonance with the aliphatic CH-stretching vibration of methylene groups at  $2850\text{ cm}^{-1}$ .

Another advantage of the presented low MHz repetition rate fiber laser design is that it enables simultaneously highly efficient generation of SHG, TPEF and CARS signals, without severely reducing the spectral resolution required for CARS microscopy, while alternative approaches are experimentally more complex, *e.g.* use either experimentally complex subsequent fs and ps excitation,<sup>24</sup> sacrifice SHG and TPEF excitation efficiency by the 80 MHz ps laser<sup>25</sup> or CARS spectral resolution by 80 MHz fs excitation.<sup>30</sup> The key parameters to describe the efficiency for the generation of nonlinear signals are the peak power of the laser and the peak intensity at the specimen. These values can be calculated using the laser repetition rate  $k$ , pulse duration  $\tau$ , the average power  $P_{\text{av}}$  and the laser spot size in the specimen plane  $A$  or the lateral resolution of the system  $d$ :

$$P_{\text{max}} = \frac{P_{\text{av}} t}{k\tau} \leftrightarrow I_{\text{max}} = \frac{P_{\text{max}}}{A} = \frac{4P_{\text{max}}}{\pi d^2} \quad (1)$$

An alternative laser for multimodal nonlinear imaging<sup>30</sup> working at similar wavelengths provides 100 fs pulses at 80 MHz repetition rate using 3.1 mW of laser power at the sample for CARS imaging generating a laser spot diameter of 310 nm. This translates according to eqn (1) to a peak power of 387 W and a peak intensity in the specimen plane of  $5 \times 10^{15}\text{ W m}^{-2}$ . The laser used in this contribution provides 20 ps pulses at 1.9 MHz repetition rate using 30 mW at the sample. This results in a peak power of 790 W and a tenfold lower peak intensity of  $5 \times 10^{14}\text{ W m}^{-2}$  in the specimen plane, while still allowing for image acquisition with a pixel dwell time of only 1  $\mu\text{s}$ . This calculation in addition to the high quality nonlinear images presented in Fig. 3–6 proves that this laser source is comparable to alternative laser sources for multimodal nonlinear microscopy in terms of the imaging performance at moderate power levels of 30 mW in the specimen plane, unless higher average powers at the sample are required, *e.g.* for imaging deeper than 100  $\mu\text{m}$  within scattering tissues. However, the spectral resolution in CARS microscopy is significantly improved in comparison to a 100 fs laser. The laser described herein provides  $40\text{ cm}^{-1}$  spectral resolution in contrast to more than  $100\text{ cm}^{-1}$  for a 100 fs 80 MHz repetition rate laser used by Chen *et al.*<sup>30</sup> In addition, further substantial improvement of the spectral resolution to  $1\text{ cm}^{-1}$  for CARS imaging is possible by seeding the FWM process.<sup>35</sup>

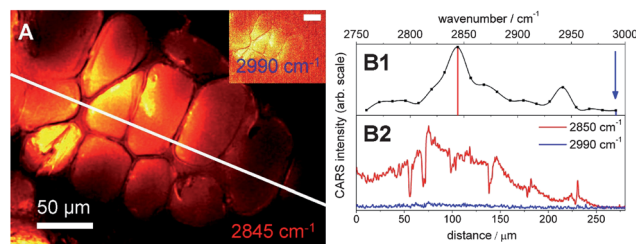


**Fig. 4** The high molecular contrast of CARS at the aliphatic C–H-stretching vibration of methylene groups when using NIR lasers is exemplarily demonstrated for adipocytes and connective tissue surrounding a human artery. In resonance the lipid droplets appear bright, while the cytoplasm and the membrane of the adipocytes are darker due to their relatively lower lipid content. The small inset shows the same image at  $2990\text{ cm}^{-1}$ . The intensity is magnified by 5 and the contrast is enhanced. In panel B1 a CARS spectrum of lipids is shown and the spectral positions for acquisition of the images in panel A and the intensity profiles of panel B2 are indicated. Panel B2 displays in and off-resonance intensity profiles. The contrast is 20 times higher in the resonant case for pure triglycerides, *i.e.* the lipid droplets in adipocytes.

Since the laser design is completely spliced and uses only polarization-maintaining fiber components<sup>37</sup> it provides unparalleled stability with respect to environmental changes. While the laser parameters differ substantially from alternative laser sources, no photodamage has been observed for this low repetition rate laser when using an average laser power of below 30 mW in the specimen plane. Thus, this light source is perfectly suited for the application in clinical settings. In summary this alignment-free turn-key laser source is due to its small footprint, insensitivity to environmental changes and simple operation combined with highly efficient CARS, SHG and TPEF signal generation ideally suited for routine clinical application.

In the following, results from imaging samples from a rabbit model for atherosclerosis and human perivascular tissue as well as tissue from an oropharyngeal squamous cell carcinoma are presented to demonstrate the systems capabilities for tissue imaging.

In Fig. 3 images from an artery tissue of a rabbit fed with a high cholesterol diet to induce atherosclerosis are displayed. In Fig. 3 panel A, a CARS image at the symmetric  $\text{CH}_2$  stretching vibration of  $2850\text{ cm}^{-1}$  for a whole artery cross-section is generated by fusing four single CARS images. It can be seen that the plaque deposits are not uniformly distributed at the vessel wall, but the plaque thickness varies across the circumference. In order to investigate areas of different plaque thickness in more detail, high resolution images have been acquired in panels B, C and D as indicated in panel A. These images visualize the curly structure of the elastic fibers of the vessel wall. The composition of the plaque is different in areas of high (Fig. 3B) and low lipid deposition (Fig. 3C). While the plaque's foam like structure appears medium intense in an area of high deposition (Fig. 3B), the plaque is more uniform in the area of thin deposition and the average CARS intensity is higher, indicating higher lipid content (Fig. 3C). To investigate these differences further, axially resolved *in vitro* imaging of a large aorta specimen with plaque deposits at the inner arterial wall

has been performed. Z projections of the lipid deposits at the inner vessel walls in areas of low and high deposition are displayed in Fig. 3 panels E and F. The CARS signal at  $2850\text{ cm}^{-1}$  corresponding to the symmetric C–H-stretching vibration of methylene groups highlights the areas of dense fatty acid deposition. While there are non-noticeable lipid deposits at the vessel wall in Fig. 3 panel E, there is an extended plaque structure exceeding  $100\text{ }\mu\text{m}$  in thickness in Fig. 1 panel F.

To demonstrate the chemical origin of the contrast of the CARS images, a sample of human perivascular tissue surrounding an artery has been investigated in resonance with the symmetric C–H-stretching vibration of methylene groups at  $2850\text{ cm}^{-1}$  and off resonance at  $2990\text{ cm}^{-1}$  as displayed in Fig. 4. In panel A of Fig. 4 the resonant image is displayed, while the inset corresponds to the off resonant image, which has been multiplied by a factor of 5 in order to visualize the adipose cells more clearly. Panel B2 displays an intensity profile along the white line shown in panel A of Fig. 4. Panel B1 displays a CARS spectrum of lipids acquired by tuning the frequency difference between the pump and Stokes lasers across the C–H-stretching region. The spectral positions for acquiring resonant and off resonant CARS images and the intensity profiles are indicated and colour coded in the CARS spectrum shown in Fig. 4 panel B1. As shown in Fig. 4 panel B2, the image contrast vanishes almost completely, if the difference frequency of the lasers is tuned off resonant. From the ratio of the intensities, the contrast has been calculated to 10. This represents only a lower bound to the Raman resonant contrast, since for low light levels a large background contribution due to noise of the readout circuit is observed. When estimating the readout noise and subtracting this contribution from the signal intensity, the image contrast is in the range of 20, which is better by a factor of 3 than for fs light sources for multimodal imaging in the same wavelength range<sup>30</sup> or even by a factor of 10 compared to the 2 ps laser system operating in the visible range.<sup>47</sup>

However, as already mentioned, the strength of the presented setup is based on the ability to not only record CARS images but also simultaneously record SHG and TPEF signals. SHG and TPEF signals are very efficiently excited in parallel to CARS, but provide information about the spatial distribution of further tissue components, in particular protein fibers,<sup>21,48</sup> oxidized fatty acids<sup>22</sup> and cholesterol.<sup>18</sup> This multitude of signals therefore provides a detailed morphochemical map of the tissue, which prospectively allows the determination of the type of atherosclerotic plaque and therefore also its risk to rupture, even without surgical excision and labelling of tissue.

In detail, TPEF displays the distribution of autofluorophores. In blood vessel walls a prominent source of autofluorescence is elastic fibers composed of the fluorescent proteins elastin and collagen.<sup>21</sup> Within atherosclerotic plaque deposits oxidized lipids are associated with fluorescence.<sup>22</sup> SHG is sensitive to highly ordered structures, which are the proteins myosin and collagen. Myosin is concentrated within the smooth muscle cells, thus especially in the blood vessel wall. Collagen is arranged in the protein fibers of connective tissue.<sup>49</sup> However, recently also different sources of SHG within lipid deposits have been reported,<sup>18</sup> especially cholesterol crystals. Therefore the multimodal

combination of these three nonlinear imaging modalities CARS, SHG and TPEF provides manifold information not only on the tissue morphology but also on the chemical composition, comparable to the information of multiple histological stains, *e.g.* the elastic van Gieson (EVG) stain for elastic fibers. This is demonstrated in Fig. 5. In panel A of Fig. 5 a multimodal image of an artery section of a rabbit fed with a high cholesterol diet is displayed combining SHG (blue), CARS at  $2850\text{ cm}^{-1}$  (red) and TPEF (green) signals to a false colour image. The individual signals are displayed in Fig. 5 panels B–D. TPEF and SHG signals, Fig. 5 panels C and D, are highly co-localized. The SHG and TPEF signals are more intense in the outermost layer, the tunica externa or tunica adventitia, which is composed of connective tissue and thus is rich in collagen, which is a source of both autofluorescence and second harmonic signals. CARS at  $2850\text{ cm}^{-1}$  visualizes the morphology of the vessel wall: the fibrous structure of the proteins and the plaque deposits. Interestingly the plaque is not uniformly rich in lipids. The highest signal intensity is visible in the outermost layer. Some bright lipid deposits are also the origin of intense SHG and TPEF signals, but not all. Therefore, cholesterol crystals and oxidized low density lipoprotein as sources of SHG and TPEF signals are not uniformly distributed within the plaque. These are interesting findings, since the plaque composition is directly related to the risk of rupture causing an acute life-threatening event like a stroke or heart attack.

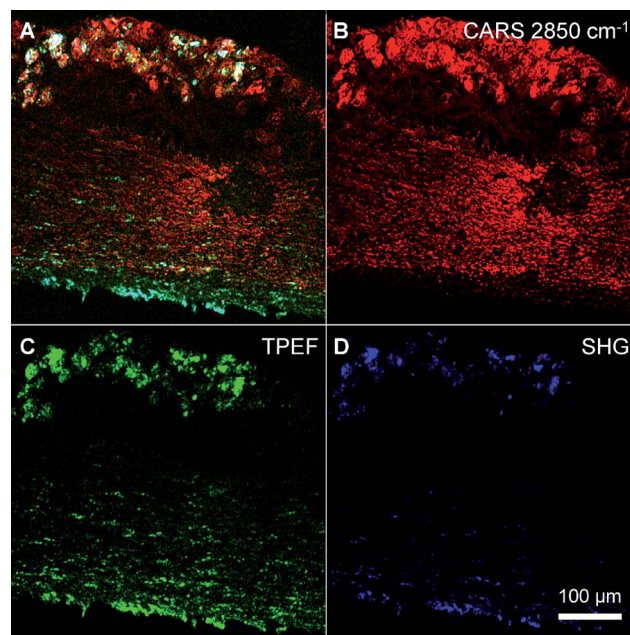


**Fig. 5** Composite multimodal nonlinear microscopic image of an artery section of an animal model for atherosclerosis. In panel A CARS, TPEF and SHG images are combined to a false colour molecular map of the artery section. CARS imaging at the symmetric C–H-stretching vibration of methylene groups at  $2850\text{ cm}^{-1}$  abundant in all major biomolecules reveals the morphology of the artery. Furthermore, it highlights lipid deposits and protein fibers due to the high concentration of scattering functional groups. TPEF in green, panel C, is used to display autofluorescent molecules, in particular fluorescent protein fibers like elastin and collagen in addition to NADPH and oxidized fatty acids in the plaques. SHG displayed in blue in panel D is sensitive to protein fibers composed of collagen and actin of smooth muscle cells, but cholesterol within the plaque does also generate signals. SHG and TPEF are co-localized to a large extent.

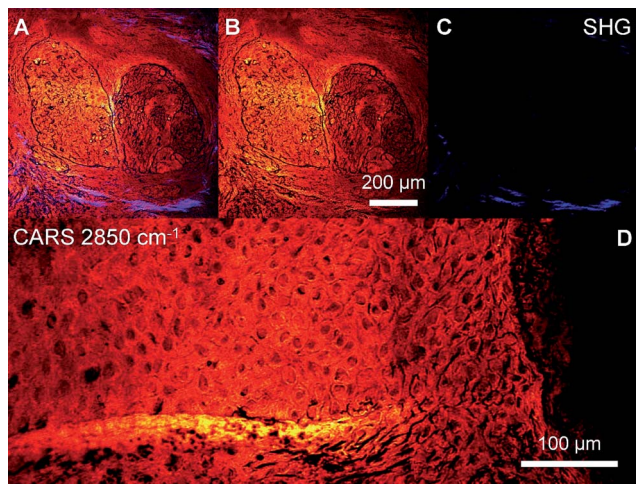


**Fig. 6** Multimodal nonlinear imaging of a head and neck squamous cell carcinoma sample from an oropharyngeal site. Panels A–C show tumor nests invasively growing into the connective tissue. In panel A both the CARS signal at the symmetric CH stretching vibration of methylene groups at  $2850\text{ cm}^{-1}$  and SHG signals of collagen fibers of the connective tissue are displayed, CARS and SHG signals are represented in panels B and C. Epithelium without pathological findings is depicted in panel D (CARS,  $2850\text{ cm}^{-1}$ ). Single epithelial cells and nuclei are visualized.

But possible clinical applications of the compact multimodal nonlinear microscope are not limited to cardiovascular diseases. This is illustrated in Fig. 6. In panels A–C of Fig. 6 multimodal images of invasively growing tumor nests of a head and neck squamous cell carcinoma sample are displayed. The tumor is growing into the connective tissue at an oropharyngeal site. In Fig. 6 panel A both the CARS signal at the symmetric CH stretching vibration of methylene groups at  $2850\text{ cm}^{-1}$  and SHG signals of collagen fibers of the connective tissue are displayed, while the single CARS and SHG signals are presented in panels B and C, respectively. In particular the visualization of collagen represents an important marker for diagnosing the transition from grade 3 to invasively growing grade 4 carcinoma. Grade 4 is defined by tumor cells breaking through the basement membrane and invading the connective tissue.<sup>3,50,51</sup> For comparison adjacent epithelium without pathological findings is depicted in panel D utilizing CARS at  $2850\text{ cm}^{-1}$ . In Fig. 6 panel D single epithelial cells and nuclei are visualized, demonstrating the potential for tissue imaging for diagnostic purposes, since grading of HNSCC relies on the visualization of architectural and cytological changes accompanying the process of carcinogenesis,<sup>50,51</sup> e.g. cell density, size and shape of individual cells and nuclei as well as the nuclei to cytoplasm ratio. Therefore also in the case of tumor diagnostics, multimodal nonlinear microscopy represents a promising imaging tool.

## Conclusions

Application of imaging tools in clinical settings poses strict constraints on the system in terms of cost effectiveness, size, complexity in handling and robustness. While the past years have seen an increasing number of studies proving that multimodal nonlinear imaging approaches are valuable tools for

illuminating aspects of disease progression at cellular and sub-cellular levels, the equipment was yet too complex for other than research applications. The compact multimodal nonlinear microscope presented herein represents a significant step towards establishing nonlinear microscopy in clinics for routine diagnostics due to its simplicity, high NIR transmission for use with low power compact lasers and a large field of view and high image quality. The instrument will be tested on disease patterns, which are directly accessible, e.g. skin cancers and head and neck cancers in the near future.

But further progress will also point to different directions, especially towards *in vivo* endoscopy. In this respect the presented fiber laser light source is not only compatible with endoscopy, but intrinsically overcomes the difficulty of coherent Raman imaging in long glass fibers and thick tissue arising from the dispersion of pulses at different wavelengths. The resulting reduction of the temporal pulse overlap with increasing fiber length is greatly reduced by using 100 ps pulses allowing for endoscope fiber lengths of a few metres without precompensation. When additional spectral information and higher spectral resolution are required, the laser source can be modified to be spectrally tunable as discussed in detail elsewhere,<sup>35</sup> resulting in a total tuning range from  $1200$  to  $3800\text{ cm}^{-1}$  and  $1\text{ cm}^{-1}$  spectral resolution. Furthermore, due to the low MHz repetition rate, this source enables both efficient SHG and TPEF imaging together with high contrast CARS microscopy, thus overcoming the discrepancy between low peak power high spectral resolution ps-lasers ideal for CARS and low spectral resolution high peak power fs-lasers ideal for TPEF and SHG, which apply to 80 MHz repetition rate oscillators.<sup>24,30</sup>

The great potential of the presented fiber laser microscope setup is exemplarily demonstrated by imaging atherosclerotic and HNSCC tissue specimens but it is explicitly not limited to examination of these particular disease patterns. The combination of SHG, TPEF and CARS imaging allows determination of the distribution of fibrous proteins, smooth muscle cells, cholesterol and lipids with spatial resolution and contrast comparable to *ex vivo* staining histopathology, but with the advantage of potentially being applicable under *in vivo* conditions in the near future. Imaging the collagen network, the collagen organization and shape is of diagnostic relevance also for grading cancer tissue.<sup>3,52,53</sup> Especially implementation into endoscopes would have the benefit of enabling *in vivo* characterization of arterial plaque depositions in order to detect high risk plaques, e.g. plaques associated with a large lipid core and a thin fibrous cap, for further monitoring or direct treatment. Also in the case of malignancies, multimodal nonlinear microscopy provides label-free excellent information on the tissue morphology and composition. During carcinogenesis first morphologic changes occur at the basement membrane. Nonlinear imaging combining depth penetrations up to 1 mm with cellular resolution is perfectly suited to detect these modifications *in vivo*. Hence, the method allows for non-invasive in-depth screening of suspicious lesions possibly reducing the number of biopsies to be taken in the future. By integration into surgical microscopes, the method may be prospectively useful for surgical guidance.

## Acknowledgements

Financial support from the European Union via the European Fonds für Regionale Entwicklung EFRE and the "Thüringer Ministerium für Bildung Wissenschaft und Kultur TMBWK" Projects: B714-07037, B578-06001, 14.90 HWP and via the European network of excellence P4L Photonics4Life as well as from the German Ministry for Science and Education BMBF MediCARS FKZ: 13N10773 & 13N10774 is highly acknowledged. M.B. acknowledges support from the Carl-Zeiss-Stiftung.

## References

- 1 S. Yue, M. N. Slipchenko and J.-X. Cheng, *Laser Photonics Rev.*, 2011, **5**, 496.
- 2 C. Krafft, B. Dietzek, M. Schmitt and J. Popp, *J. Biomed. Opt.*, 2012, **17**, 40801.
- 3 T. Meyer, O. Guntinas-Lichius, F. von Eggeling, G. Ernst, D. Akimov, M. Schmitt, B. Dietzek and J. Popp, *Head & Neck*, 2012, DOI: 10.1002/hed.23139.
- 4 R. Cicchi, S. Sestini, V. De Giorgi, D. Massi, T. Lotti and F. S. Pavone, *J. Biophotonics*, 2008, **1**, 62.
- 5 F. Helmchen and W. Denk, *Nat. Methods*, 2005, **2**, 932.
- 6 D. Kobat, M. E. Durst, N. Nishimura, A. W. Wong, C. B. Schaffer and C. Xu, *Opt. Express*, 2009, **17**, 13354.
- 7 J. L. Suhailim, J. C. Boik, B. J. Tromberg and E. O. Potma, *J. Biophotonics*, 2012, **5**, 387.
- 8 C. L. Evans, X. Xu, S. Kesari, X. S. Xie, S. T. C. Wong and G. S. Young, *Opt. Express*, 2007, **15**, 12076.
- 9 T. Meyer, N. Bergner, C. Bielecki, C. Krafft, D. Akimov, B. F. M. Romeike, R. Reichart, R. Kalff, B. Dietzek and J. Popp, *J. Biomed. Opt.*, 2011, **16**, 21113.
- 10 T. Meyer, N. Bergner, A. Medyukhina, B. Dietzek, C. Krafft, B. F. M. Romeike, R. Reichart, R. Kalff and J. Popp, *J. Biophotonics*, 2012, **5**, 729.
- 11 C. Krafft, A. A. Ramoji, C. Bielecki, N. Vogler, T. Meyer, D. Akimov, P. Rösch, M. Schmitt, B. Dietzek and J. Popp, *J. Biophotonics*, 2009, **2**, 303.
- 12 N. Vogler, T. Meyer, D. Akimov, I. Latka, C. Krafft, N. Bendsoe, K. Svanberg, B. Dietzek and J. Popp, *J. Biophotonics*, 2010, **3**, 728.
- 13 T. T. Le, S. Yue and J.-X. Cheng, *J. Lipid Res.*, 2010, **51**, 3091.
- 14 *Todesursachen in Deutschland*, Statistisches Bundesamt, Wiesbaden, 2011.
- 15 R. P. Choudhury, V. Fuster and Z. A. Fayad, *Nat. Rev. Drug Discovery*, 2004, **3**, 913.
- 16 D. R. J. Owen, A. C. Lindsay, R. P. Choudhury and Z. A. Fayad, *Annu. Rev. Med.*, 2011, **62**, 25.
- 17 K. Schenke-Layland, *J. Biophotonics*, 2008, **1**, 451.
- 18 J. L. Suhailim, C.-Y. Chung, M. B. Lilledahl, R. S. Lim, M. Levi, B. J. Tromberg and E. O. Potma, *Biophys. J.*, 2012, **102**, 1988.
- 19 R. Cicchi, N. Vogler, D. Kapsokalyvas, B. Dietzek, J. Popp and F. S. Pavone, *J. Biophotonics*, 2013, **6**, 129.
- 20 A. C.-T. Ko, A. Ridsdale, L. B. Mostaco-Guidolin, A. Major, A. Stolow and M. G. Sowa, *Biophys. Rev.*, 2012, **4**, 323.
- 21 ed. M. Monici and M. R. El-Gewely, *Cell and tissue autofluorescence research and diagnostic applications*, Elsevier, 2005, pp. 227–256.
- 22 K. Arakawa, K. Isoda, T. Ito, K. Nakajima, T. Shibuya and F. Ohsuzu, *Arterioscler., Thromb., Vasc. Biol.*, 2002, **22**, 1002.
- 23 J. P. Pezacki, J. A. Blake, D. C. Danielson, D. C. Kennedy, R. K. Lyn and R. Singaravelu, *Nat. Chem. Biol.*, 2011, **7**, 137.
- 24 T. T. Le, I. M. Langohr, M. J. Locker, M. Sturek and J.-X. Cheng, *J. Biomed. Opt.*, 2007, **12**, 54007.
- 25 H.-W. Wang, I. M. Langohr, M. Sturek and J.-X. Cheng, *Arterioscler., Thromb., Vasc. Biol.*, 2009, **29**, 1342.
- 26 A. C. T. Ko, A. Ridsdale, M. S. D. Smith, L. B. Mostaco-Guidolin, M. D. Hewko, A. F. Pegoraro, E. K. Kohlenberg, B. Schattka, M. Shiomi, A. Stolow and M. G. Sowa, *J. Biomed. Opt.*, 2010, **15**, 20501.
- 27 L. B. Mostaco-Guidolin, A. C.-T. Ko, D. P. Popescu, M. S. D. Smith, E. K. Kohlenberg, M. Shiomi, A. Major and M. G. Sowa, *Phys. Med. Biol.*, 2011, **56**, 5319.
- 28 C. Matthäus, S. Dochow, G. Bergner, A. Lattermann, B. F. M. Romeike, E. T. Marple, C. Krafft, B. Dietzek, B. R. Brehm and J. Popp, *Anal. Chem.*, 2012, **84**, 7845.
- 29 T. Meyer, D. Akimov, N. Tarcea, S. Chatzipapadopoulos, G. Muschiolik, J. Kobow, M. Schmitt and J. Popp, *J. Phys. Chem. B*, 2008, **112**, 1420.
- 30 H. Chen, H. Wang, M. N. Slipchenko, Y. Jung, Y. Shi, J. Zhu, K. K. Buhman and J.-X. Cheng, *Opt. Express*, 2009, **17**, 1282.
- 31 H. Kano and H. Hamaguchi, *Opt. Express*, 2006, **14**, 2798.
- 32 G. Krauss, T. Hanke, A. Sell, D. Träutlein, A. Leitenstorfer, R. Selm, M. Winterhalder and A. Zumbusch, *Opt. Lett.*, 2009, **34**, 2847.
- 33 A. F. Pegoraro, A. Ridsdale, D. J. Moffatt, J. P. Pezacki, B. K. Thomas, L. Fu, L. Dong, M. E. Fermann and A. Stolow, *Opt. Express*, 2009, **17**, 20700.
- 34 S. Lefrançois, D. Fu, G. R. Holtom, L. Kong, W. J. Wadsworth, P. Schneider, R. Herda, A. Zach, X. Sunney Xie and F. W. Wise, *Opt. Lett.*, 2012, **37**, 1652.
- 35 M. Chemnitz, M. Baumgartl, T. Meyer, C. Jauregui, B. Dietzek, J. Popp, J. Limpert and A. Tünnermann, *Opt. Express*, 2012, **20**, 26583–26595.
- 36 M. Baumgartl, M. Chemnitz, C. Jauregui, T. Meyer, B. Dietzek, J. Popp, J. Limpert and A. Tünnermann, *Opt. Express*, 2012, **20**, 4484.
- 37 M. Baumgartl, T. Gottschall, J. Abreu-Afonso, A. Diez, T. Meyer, B. Dietzek, J. Rothhardt, J. Popp, J. Limpert and A. Tünnermann, *Opt. Express*, 2012, **20**, 21010.
- 38 T. Gottschall, M. Baumgartl, A. Sagnier, J. Rothhardt, C. Jauregui, J. Limpert and A. Tünnermann, *Opt. Express*, 2012, **20**, 12004.
- 39 X. L. Nan, E. O. Potma and X. S. Xie, *Biophys. J.*, 2006, **91**, 728.
- 40 S. Bégin, B. Burgoyne, V. Mercier, A. Villeneuve, R. Vallée and D. Côté, *Biomed. Opt. Express*, 2011, **2**, 1296.
- 41 M. D. Abramoff, P. J. Magalhães and S. J. Ram, *Biophotonics International*, 2004, **11**, 36.
- 42 J. X. Cheng, A. Volkmer and X. S. Xie, *J. Opt. Soc. Am. B*, 2002, **19**, 1363.

- 43 F. Ganikhanov, S. Carrasco, X. S. Xie, M. Katz, W. Seitz and D. Kopf, *Opt. Lett.*, 2006, **31**, 1292.
- 44 N. Dudovich, D. Oron and Y. Silberberg, *Nature*, 2002, **418**, 512.
- 45 Y.-H. Zhai, C. Goulart, J. E. Sharping, H. Wei, S. Chen, W. Tong, M. N. Slipchenko, D. Zhang and J.-X. Cheng, *Appl. Phys. Lett.*, 2011, **98**, 191106.
- 46 T. B. Huff, Y. Shi, Y. Fu, H. Wang and J.-X. Cheng, *IEEE J. Sel. Top. Quantum Electron.*, 2008, **14**, 4.
- 47 G. Bergner, S. Chatzipapadopoulos, D. Akimov, B. Dietzek, D. Malsch, T. Henkel, S. Schlücker and J. Popp, *Small*, 2009, **5**, 2816.
- 48 W. R. Zipfel, R. M. Williams, R. Christie, A. Y. Nikitin, B. T. Hyman and W. W. Webb, *Proc. Natl. Acad. Sci. U. S. A.*, 2003, **100**, 7075.
- 49 P. Campagnola, *Biophys. J.*, 2002, **82**, 493.
- 50 J. P. Sapp, L. Eversole and G. Wysocki, *Contemporary Oral and Maxillofacial Pathology*, Elsevier, 2003, p. 464.
- 51 J. Reibel, *Crit. Rev. Oral Biol. Med.*, 2003, **14**, 47.
- 52 A. Medyukhina, N. Vogler, I. Latka, S. Kemper, M. Böhm, B. Dietzek and J. Popp, *J. Biophotonics*, 2011, **4**, 627.
- 53 R. Cicchi, D. Kapsokalyvas, V. D. Giorgi, V. Maio, A. V. Wiechen, D. Massi, T. Lotti and F. S. Pavone, *J. Biophotonics*, 2010, **3**, 34.